Improving orbit prediction via thermospheric density calibration

Callejon Cantero, M.; Pastor-Rodriguez, A.; Siemes, C.

Publication date
2023

Document Version
Final published version

Published in
Proceedings of the 2nd NEO and Debris Detection Conference, Darmstadt, Germany, 24-26 January 2023

IMPROVING ORBIT PREDICTION VIA THERMOSPHERIC DENSITY CALIBRATION

M. Callejón Cantero[(1)], A. Pastor[(1)], and C. Siemes[(2)]

[(1)]*GMV, Isaac Newton 11, 28670, Tres Cantos, Madrid, Spain, Email: {miguel.callejon.cantero, apastor}@gmv.com*
[(2)]*Faculty of Aerospace Engineering, Kluyverweg 1, 2629HS, Delft University of Technology, Delft, The Netherlands, Email: c.siemes@tudelft.nl*

ABSTRACT

The uncertainty on Thermospheric Mass Density (TMD), as derived from atmospheric models, can reach values up to $30\,\%$. This effect is noteworthy in Low Earth Orbit (LEO), where drag is the main perturbing force. Furthermore, LEO regime harbours more than 17500 objects at the end of 2021, almost $60\,\%$ of tracked objects orbiting Earth, and the rate of growth raises every year. Increasing the accuracy of density models, and thus characterizing better the uncertainty of an orbit, is needed to ensure space environment sustainability in a crowded environment. This paper presents an approach for assimilating thermospheric density observations into atmospheric models to improve the accuracy of orbit predictions in orbit propagations over a length of up to 10 days. First, Global Navigation Satellite Systems (GNSS) derived density data from Swarm satellites are ingested from the publicly available Level 2 ESA data products. Then, density data is assimilated into the empirical model NLRMSISE-00, using Principal Component Analysis (PCA) to decompose a fine grid in density into the main temporal and spatial modes, which provides insight into the physical variation of the model. Thirdly, the model is verified by applying it to other satellites, whose data was not assimilated, such as GRACE-FO satellites. The preliminary results obtained show that a simple Weighted Least Squares Estimation (WLSE) can fit all density observations of one month, and correctly predict the density during the next month. However, when propagating a satellite with an estimable drag coefficient C_D and precisely known ephemeris, the benefits of propagating using the calibrated model are overshadowed when performing an orbital fit of the dynamical model to the ephemeris.

1. INTRODUCTION

Atmospheric drag is the main perturbation force acting on space objects on LEO under $1000\,\mathrm{km}$, excluding Earth's non-spherical gravity field. Despite this, the uncertainty in satellite drag modelling is large compared to other perturbing forces. The uncertainty sources on drag derive from imprecise knowledge of the object's shape and position; the wind acting on the object, which affects its inertial velocity; the aerodynamic coefficients of the object, either from an imperfect geometric model or an imperfect characterization of the gas-surface interaction; and the true physical TMD in the atmosphere. Several models exist that characterize the density in the upper layers of the atmosphere, but the uncertainty on the computed TMD can reach values up to $30\,\%$, or even higher. The accuracy of the models can be improved by assimilating atmospheric density observations retrieved from Precise Orbit Determination (POD) ephemeris of LEO satellites. Therefore, accurate thermosphere modelling is a decisive factor in all space applications below the exopause: from LEO mission design, re-entry trajectory design, to POD, Space Situational Awareness (SSA), or collision avoidance in Space Traffic Management (STM). The relevance for space debris risk mitigation is especially noteworthy, as the LEO region harbours the vast majority of space objects tracked [13, 23].

The physical environment of the upper layers of the atmosphere is quite complex to model. Solar Extreme Ultraviolet (EUV) radiation, as well as coronal mass ejections, drive the temperature at the thermosphere, the composition of the exosphere, and the resulting density [9]. Both phenomena are characterized by space weather proxies. For the heating of the atmosphere, caused by the EUV radiation, $F_{10.7}$ proxy is usually used. It represents the daily solar radio flux density at a wavelength of $10.7\,\mathrm{cm}$, which can vary between $70\,\mathrm{sfu}$ to $370\,\mathrm{sfu}$ [19] depending on the solar activity, which alternates in cycles of $11\,\mathrm{years}$. The mean 81-day value of $F_{10.7}$ is also used in several thermospheric models, as well as an adjusted proxy $F_{10.7,ADJ}$ to exactly match one astronomical unit distance. Other indices are also used to better account for solar heating [2, 4] such as F_{30}, the solar flux at a wavelength of $30\,\mathrm{cm}$; M_{10}, which measures the ratio of solar Mg II emission scaled to $F_{10.7}$ units; the solar flux at $26\,\mathrm{nm}$ to $34\,\mathrm{nm}$ S_{10}; or the mixed index Y_{10}, which accounts for the solar flux at $121.57\,\mathrm{nm}$ and solar X-ray radiation, that dominate at low and high solar activity, respectively. Coronal mass ejections and solar wind, on the other hand, highly affect the thermosphere during geomagnetic storms due to complex interactions with the magnetosphere and ionosphere [7, 8]. The proxies a_P and K_p are usually used to account

Proc. 2nd NEO and Debris Detection Conference, Darmstadt, Germany, 24-26 January 2023, published by the ESA Space Safety Programme Office
Ed. T. Flohrer, R. Moissl, F. Schmitz (http://conference.sdo.esoc.esa.int, February 2023)

for geomagnetic activity, which measures the variation of geomagnetic field with different scales [19]. The disturbance storm time D_{st} indicates the intensity of the horizontal magnetic field at the storm-time ring current, which is highly energized during magnetic storms [3].

When predicting the TMD in the close future, any uncertainty on these parameters correlates to the density, and afterwards to the drag. Therefore, it is crucial to have a realistic uncertainty characterization of existing parameters. Also, if the proxies are predicted, as in a short- or medium-term propagation (propagation over days, up to one month), an extra source of uncertainty on the density inputs arises: the proxies are not a measurement, but the prediction of a solar proxy. Sáez and Escobar [37] performed a statistical analysis of $F_{10.7}$ and a_P proxies. For $F_{10.7}$, a higher uncertainty on high solar activity was found and, regardless of the solar activity, $F_{10.7}$ uncertainty (1σ equivalent) could be bound to $5\,\%$ for one-day prediction, and, for a_P, no correlation with the solar activity was found, and a_P uncertainty could be bound to $50\,\%$. Licata et al. [24] analysed the uncertainty of the drivers for several solar and geomagnetic combinations and propagated a small theoretical satellite at three altitudes. The standard deviation of in-track position error is higher at lower altitudes and grows with increasing solar and geomagnetic activity. $F_{10.7}$ was found to have a greater impact on the propagation than a_P.

Spatial variation of TMD accounts for several physical phenomena. The vertical variation is approximated by the exponential decay from hydrostatic equilibrium with an uncertainty estimated to be around $3.5\,\%$ at $400\,\mathrm{km}$ in geomagnetic calm periods, which may be highly underestimated in geomagnetic storms [19]. The International Standard Atmosphere [21] model is based on this formula, which is more accurate at lower altitudes. The horizontal variation is caused by several factors, such as global atmospheric circulation, variation in the Earth's gravity field due to tides, Sun-Earth distance, Joule heating, solar flux, or solar wind [19]. Latitudinal and longitudinal variations are usually coupled, as with the Equatorial Mass Density Anomaly: a two-cell structure with two crests around the geomagnetic latitude of $25°$ to $30°$ and a dip at the geomagnetic equator [19]. Furthermore, PCA analysis suggests that the spatial distribution of the TMD varies with diurnal, semi-diurnal, and higher harmonic terms of the motion of the Sun and the corresponding heating of the atmosphere [29].

State-of-the-art models of the upper atmosphere can be categorized into two groups: physics-based models and semi-empirical models. Physics-based models, such as the Global ionosphere–thermosphere model (GITM; 36), and the Thermosphere-Ionosphere-Electrodynamics General Circulation Model (TIE-GCM; 35), solve the full continuity, momentum, and energy Navier-Stokes equations for either neutral or charged particles in a three-dimensional grid. The difference between both models lies in using different advection equations: TIE-GCM assumes hydrostatic equilibrium, while GITM solves for a non-hydrostatic thermosphere, and GITM also includes the divergence of all velocity terms. On the other hand, semi-empirical models, such as the US Naval Research Laboratory mass spectrometer and incoherent scatter radar exosphere model - 2000 (NRLMSISE-00; 34), the Drag Temperature Model - 2013 (DTM2013; 4), or Jacchia-Bowman - 2008 (JB08; 2), are based on equations of thermal and diffusive equilibrium on the atmosphere. Afterwards, these models are fitted in the least squares sense to large datasets which give more accurate measurements of atmospheric density. NRLMSISE-00 database includes the database of previous MSIS-class models, i.e., ground-, rocket-, and satellite-based measurements, as well data from MSISE-90, which include sources from Incoherent Scatter Radar, mass spectrometer, and others. NRLMSISE-00 was the first MSIS-class model that also included drag measurements and satellite-borne accelerometer datasets. It uses the solar indices $F_{10.7}$ and a_P as proxies of the solar flux and geomagnetic activity, respectively. JB08 and DTM2013 models use a different set of indices: $F_{10.7}$, S_{10}, M_{10}, Y_{10}, and D_{st} are used in JB08, and F_{30} and K_p are used in DTM2013. Each model was tuned assimilating data from different sources, for example, Jacchia orbital drag, CHAMP, GRACE, and GOCE accelerometer-derived satellites. JB08 model assimilated densities from the High Accuracy Satellite Drag Model (HASDM; 38) obtained with the Dynamic Calibration Atmosphere procedure, and therefore represents more closely HASDM derived density, especially during geomagnetic storms [2]. All models overestimate Solar Ultraviolet flux during solar minima, while DTM2013 and JB08 are more precise compared to the observations of the satellites that were part of the construction of the model [4]. In the case of DTM2013, the augmented precision can be related to using an internally consistent scale: there is neither a consensus nor a standard on the drag coefficient C_D and ballistic coefficient BC used to derive the final density [6, 19]. Differences within the models cause a bias related to the satellite model used, which can vary both in geometric shape differences and gas-surface interaction. NRLMSISE-00 [12] and DTM2020 [5] have been recently updated, including a more detailed physical description of the lower thermosphere ($70\,\mathrm{km}$ to $200\,\mathrm{km}$) and assimilating density data from more sources, respectively. Nevertheless, not of these models presents a clear advantage over the others in a generic configuration (as in not limited to particular orbits): DTM2013 and JB08 are usually more accurate, but they require solar indices that are not available in a real-time operational set-up [19, 32, 39].

Current trends to reduce uncertainty in the drag atmospheric modelling include calibrating these models with new and more accurate satellite observations, which are still very sparse [5, 28]. The broad database of Two-Line Elements (TLE) has been used to calibrate TMD semi-empirical models and improve the Root Mean Squared (RMS) density model error from $30\,\%$ to $15\,\%$ [11]. Some studies employed the TLE of decaying satellites to compare the bias of semi-empirical models

[32]. More recently, Unscented Kalman Filter (UKF) was used to assimilate TLE data in real-time into a dynamical Reduced-Order Model of NRLMSISE-00, JB08, and TIE-GCM models [17]. The accuracy in density was in general improved. Along the CHAMP orbit, whose TLE data was included in the model, the RMS of density error improved from $26.7\,\%$ to $7.7\,\%$. However, it was also concluded that assimilating precise density data instead of carefully chosen TLE elements might improve the model.

Radar and GPS density measurements have also been used to calibrate empirical models [18, 10, 44]. Artificial Neural Networks have been suggested as a method to include density observations into a model to improve its accuracy and prediction capabilities [25, 33]. A predictor localized on certain orbits was proposed in [33], while a model based on HASDM dataset that accurately represents the dataset was generated by [25]. Kalman's filters have been used to assimilate atmospheric data into a physics-based model GITM [22, 31]. While a UKF was used in [22] to assimilate atmospheric composition data into the model in localized parts of the grid, CHAMP density measurements were assimilated in [31] using an Ensemble Kalman Filter (EnKF), reducing its bias. Fitting the semi-empirical models' output density to a linear regression has also been proposed [1] to afterwards assimilate, using a Kalman filter, Swarm-C and GOCE satellite measurements into a state composed of the linear regression coefficients.

CHAMP and GRACE accelerometer-derived measurements have been assimilated [15] using an EnKF and an Ensemble Square-Root Kalman Filter that modifies, at each analysis step, a set of density estimations and the four NRLMSISE-00 parameters that influenced the most the model after a Global Sensitivity Analysis: $F_{10.7}$, a_P, and two internal model coefficients that affect the upper exospheric temperature T_{ex}: `ptm[0]` and `pt[0]` [15]. The definition of T_{ex} and its relation with the model can be found in literature [20], and the relation with the model coefficients can be found in NRLMSISE-00 source code. The model was tuned to the TMD estimates during the entire year of 2003, and an improvement of $27\,\%$ reduction of RMS between the model and observations was achieved. Forootan et al. [15] discussed how their method can be further extended, and implemented operationally, using GRACE and Swarm measurements.

The swarm mission was launched on 22 November 2013 by the European Space Agency (ESA) with the main goal of measuring the Earth's magnetic field and how it interacts with the Earth [16]. In addition, GNSS and accelerometer measurements of Swarm allow for obtaining very precise measurements of density along its orbit [40, 42]. The swarm constellation is formed of three satellites: Swarm-B flies at an altitude of $510\,\mathrm{km}$, while the other two identical satellites fly side-by-side at a lower initial altitude of $480\,\mathrm{km}$. An updated chain has been proposed [40] based on GNSS, a very precise geometrical model, and a realistic aerodynamic model for rarefied gas. The density data output sampled in $30\,\mathrm{s}$ with a resolution of $20\,\mathrm{min}$, and stored in $24\,\mathrm{h}$ files [40]. The resulting observations were validated with a statistical comparison with NRLMSISE-00, which confirms the over-predicting bias of the model, and how the new method augments the correlation with the model. The obtained densities are available as a ESA Level 2 product, and could be produced in real-time in the future [private communication, C. Siemes, 2022]. Thus, as suggested by previous literature, implementing a real-time assimilation approach of Swarm densities into NRLMSISE-00 model might improve the model accuracy and highly benefit SSA and space debris risk mitigation.

The novelty of this ongoing work consist on assessing the capabilities of assimilating density data into NRLMSISE-00 model with two objectives: 1) predicting the density at future epochs, and 2) assessing the possible benefits of propagating a typical scenario using the calibrated model over a period of up to one week. First, a first step in assimilating Swarm densities into NRLMSISE-00 model is taken. NRLMSISE-00 has been decomposed in its main components using PCA [14, 29]. For that, a grid of NRLMSISE-00 has been created in longitude, latitude, and time. Second, each principal component has been calibrated using WLSE procedure with Swarm-C density observations. The model has been validated with training data by analysing the residuals of the fit, and its prediction capabilities have been tested. Finally, the calibrated density model has been tested in several scenarios, comparing the propagation of two precisely known objects: satellites Swarm-C and GRACE-FO-1. Present work is divided into three sections: in section 2, the particularities of each method used are explained, in section 3, the calibration, prediction, and propagation output are analysed, and finally, in section 4, the conclusions and future work are outlaid.

2. METHODOLOGY

The methodology employed in this study involves using WLSE to fit NRLMSISE-00 model to the atmospheric density observations of the Swarm-C satellite. WLSE method is a commonly used technique for fitting a mathematical model to a set of observations and is chosen for its simplicity and robustness. This section is divided into two subsections: subsection 2.1, which describes the procedure for calibrating and predicting the NRLMSISE-00 model using WLSE and subsection 2.2, which outlines the design of test cases to evaluate the accuracy of the calibrated model.

2.1. Density calibration and prediction

The NRLMSISE-00 model has been sampled using PCA in longitude, latitude and time. This approach involves analysing the data to identify patterns and variations in the atmospheric density at different locations, times and

seasons. PCA allows identifying the main directions of variation in both the spatial and temporal domains. Spatial discretization was on a grid with 80 points in longitude and 40 points in latitude. The time grid collected a sample every 10 minutes for one month. This grid size and sampling frequency provide a high-resolution representation of the atmospheric density at different locations and times in a matrix $\mathbf{X}_{grid}$ of size 4464×3200, allowing for a detailed analysis of the patterns and variations in the data.

Using a high-resolution grid and a fine time sampling allows capturing the small-scale variations in the atmosphere, which can be useful for different applications. Additionally, the one-month time sampling allows considering the monthly and diurnal variations in the atmosphere. This sampling strategy ensures that the model is representative of the Earth's atmosphere under certain conditions (a particular level of solar heating, altitude close to that of Swarm-C orbit) and provides a detailed understanding of the atmospheric density at different locations and times. Coarser resolution grids have been tested in the calibration process, but the results were not as accurate as the 80x40 grid used. While the resolution can be further smoothed, the accuracy of the model is already sufficient and an increase in computation time would be incurred.

Regarding altitude discretization, there are several options. It is possible to add a third dimension to the spatial grid, by making the grid coarser, as in [29]. However, it is also possible to use the vertical variation profile as in the NRLMSISE-00 model [15, 34]. Although this hypothesis might add non-negligible differences during geomagnetic storms [19], the added error is assumed to be far below the model error during the present work. The vertical variation profile can be computed as:

$$\rho_h = \rho_{400} \frac{\rho_{M,h}}{\rho_{M,400}}, \tag{1}$$

where subscript M represents NRLMSISE-00 model, and 400 represents density at altitude of $400\,\mathrm{km}$. Therefore, NRLMSISE-00 grid is created at an altitude of $400\,\mathrm{km}$, and density at any other height is computed with Equation 1.

The input of NRLMSISE-00 was chosen according to the recommendations in the literature [34, 39]. This involved using actual observed values for $F_{10.7}$ and a_P indices instead of predicted ones. This allows for a more accurate representation of the current atmospheric conditions. Additionally, 3-hourly a_P indices were used, which capture the small-time-scale variations in the atmosphere better than one-day a_P indices. Furthermore, the $F_{10.7}$ values were adjusted to exactly $1\,\mathrm{AU}$. The use of observed values for indices, 3-hourly a_P and adjusted $F_{10.7}$ values have been found to improve the model's accuracy [39].

PCA is a technique used to analyse and reduce the dimensionality of a dataset, it is often used in the context of atmospheric density data. $\mathbf{X}_{grid}$ is decomposed in its main components, such that:

$$\mathbf{X}_{grid} = \bar{\mathbf{X}}(\mathbf{s}) + \mathbf{U} \cdot \mathbf{S} \cdot \mathbf{V}^T = \bar{\mathbf{X}}(\mathbf{s}) + \mathbf{P}(t) \cdot \mathbf{E}(\mathbf{s}) \tag{2}$$

In Equation 2, time variation t of the components is retained in matrix $\mathbf{P}(t)$, while space matrix $\mathbf{E}(\mathbf{s})$ retains information about the spatial grid $\mathbf{s}$. Matrix $\bar{\mathbf{X}}(\mathbf{s})$ contains the mean spatial value of each component, and $\mathbf{U}$, $\mathbf{S}$, and $\mathbf{V}^T$ matrices are the output of Singular Value Decomposition [43] factorization, the core of PCA algorithm. The components are sorted in descending order of their variance. The first component has the highest variance, and each subsequent component has a lower variance. This is because, by sorting by eigenvalues, the directions (components) in the data that have the most variation (or information) are found, and the data is projected onto these directions. By sorting the components in this way, the first few components will account for the majority of the variation in the data, and the remaining components will account for less and less variation.

The amount of information that is retained using PCA can be measured with the normalized eigenvalues, i.e., each component of matrix $\mathbf{S}$ divided by the summation of all the eigenvalues in a PCA with all possible components (in this case, 3200, the spatial grid size). The data can be represented in fewer dimensions without losing information: with 10 components, $92.89\,\%$ of the information is retained; with 15 components, $96.53\,\%$, and with 20 components, $98.08\,\%$. For a comprehensive overview of PCA, the reader is directed to [14, 15, 29, 43].

PCA matrices of atmospheric density are generated using the NRLMSISE-00 model. However, it is acknowledged that models can be subject to errors and biases. To enhance the accuracy of NRLMSISE-00, a calibration process has been implemented using the WLSE algorithm in conjunction with observations of the Swarm-C satellite. The Swarm satellite mission provides highly precise observations of the atmosphere, which are considered to be state-of-the-art in terms of atmospheric density knowledge. These observations have been extensively used as ground-truth data in various studies [5, 1] and are readily available to the public. To validate the proper importation of the dataset, the density histograms were compared with literature [40].

The calibration has been performed using WLSE [30] to estimate the parameters $\mathbf{y} = [\mathbf{y}_{PCA}, y_{mean}]$, where $\mathbf{y}_{PCA}$ is a vector containing scale factors of the PCA components, and y_{mean} is the scale factor for the mean [15, section 2.3.2]:

$$\mathbf{X}_{calibr} = y_{mean}\bar{\mathbf{X}}(\mathbf{s}) + \mathbf{P}(t) \cdot \mathrm{diag}(\mathbf{y}_{PCA}) \cdot \mathbf{E}(\mathbf{s}) \tag{3}$$

Previous equation is linear with respect to the estimated parameters, and thus it can be solved with a linear

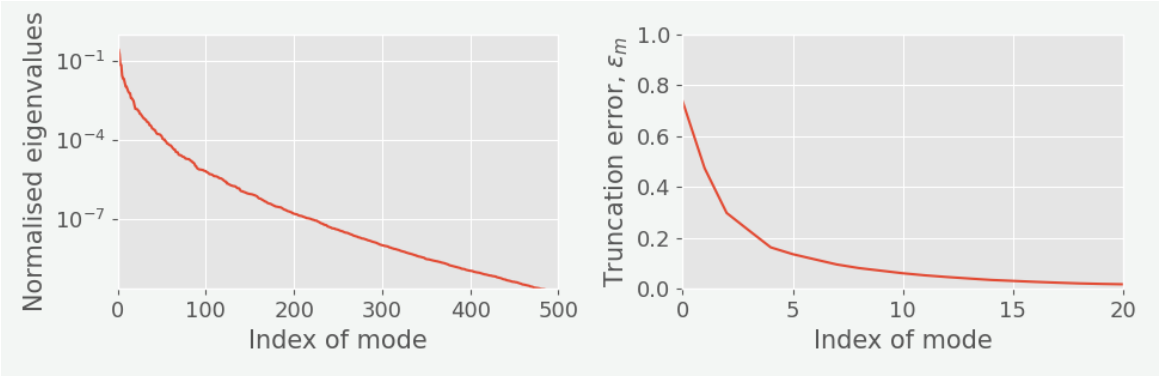

Figure 1: Normalized eigenvalues of X_{grid} and truncation error in the 10 first components.

WLSE, as in [15]. Non-linear WLSE method [30] can be mathematically represented as:

$$\mathbf{y}^{(k+1)} = \mathbf{y}^{(k)} + (\mathbf{H}^T\mathbf{W}\mathbf{H})^{-1}\mathbf{H}^T\mathbf{W}\Delta\mathbf{z} \qquad (4)$$

where k is the iteration number, $\mathbf{p}$ contains the parameters that are not estimated, $\mathbf{H} = \dfrac{\partial h(t, \mathbf{y}, \mathbf{p})}{\partial y_i}$ is the Jacobian of the measurement function $\mathbf{h} = \hat{\mathbf{z}} = \hat{\mathbf{x}}$, $\mathbf{x}$ is the state, in this case, the logarithm of the density $\mathbf{x} = \ln \boldsymbol{\rho}$, $\mathbf{W}$ is the diagonal matrix of measurement weights, and $\Delta\mathbf{z}$ are the residuals to minimize. This linearization procedure has obtained the same results as the direct method from [15]. The matrix $\mathbf{P} = \left(\mathbf{H}^T\mathbf{W}\mathbf{H}\right)^{-1}$ denotes the covariance matrix of the parameters, a measurement of the confidence in the solution.

This calibration process is expected to significantly improve the precision of the NRLMSISE-00 model. To provide a dense grid over the period that is being calibrated, matrices $\bar{\mathbf{X}}(\mathbf{s})$, $\mathbf{P}(t)$, and $\mathbf{E}(\mathbf{s})$ are interpolated at a certain point in time and space (longitude and latitude).

Two interpolators have been compared: a Radial Basis Functions (RBF) interpolator, and a grid interpolator based on the Clough Toucher (CT) algorithm. Both are available in the open-source library SciPy [41]. Both RBF and CT have been shown to effectively interpolate within acceptable error margins: RBF has a $4.06 \cdot 10^{-5}$ relative error, and CT $7.74 \cdot 10^{-5}$. For the prediction and calibration of the density, RBF has been used. However, for the orbital propagation, a simple bi-dimensional method has been created based on one-dimensional Lagrange interpolators. The method first interpolates on one dimension and solves N points. Afterwards, it interpolates along the second dimension using as nodal points the N points previously computed. Both interpolators add an associated error below the expected intrinsic error of the density model.

Finally, the calibration has been tested for predicting atmospheric densities during the period following the calibration. It has been assumed that all the inputs of NRLMSISE-00 are available during the close future (i.e., all indices are available, and the error due to a predicted solar index is not taken into account). Thus, matrices $\bar{\mathbf{X}}(\mathbf{s})$, $\mathbf{P}(t)$, and $\mathbf{E}(\mathbf{s})$ are available for the real future, and parameters $\mathbf{y}$ are calibrated with the prior month. The residuals of the prediction are analysed in section 3.

2.2. Orbital propagation with Calibrated model

The calibrated model has afterwards been tested in the propagation of a LEO orbit to assess and quantify the advantages of the calibration with satellite observations. Therefore, in a real-time scenario, a calibrated model might be able to present benefits in terms of better characterization of an orbit. Two-time frames have been tested: one with very low solar activity, January 2019, and one with mild solar activity, March 2022. The calibrated model has been tested in two satellites: Swarm-C, and GRACE-FO-1. Swarm-C case is expected to be the best-case scenario: its density observations have been assimilated. On the other hand, GRACE-FO-1 is a realistic test case for an operational satellite with a stable, well-controlled attitude, and known POD ephemeris. There are also differences between both satellites' altitude and local-solar time, due to the different orbit: Swarm-C flies at an approximate altitude of $480\,\mathrm{km}$, while GRACE-FO-1 at $500\,\mathrm{km}$.

The orbital propagation has two steps. First, an orbital fit is performed during a short period (3 days). The fit is a WLSE process in which the initial position, velocity, drag coefficient C_D and radiation coefficient C_R of the satellite that minimizes the residuals concerning a POD orbit are found. In the second step, the orbit is propagated for one week using the initial step found during the fit. The objective of the fit is to minimize any discrepancies in the dynamical model used to obtain POD orbit and one used when propagating so that the dynamical model that was used to retrieve POD observations does not affect the propagation.

The propagation uses a typical LEO dynamical environment for the propagation: non-spherical harmonics with degree and order 64, solid tides, drag force, Solar Radiation Pressure (SRP), and third body effects of the Sun, the Moon, and J2 harmonic of

the Moon as perturbations. It is noteworthy that the C_D which is the output of the previous fit will compensate partially the calibration performed in the density, as drag is described by Equation 5 and the acceleration shall be the same to fit the dynamical model to the observations.

$$\mathbf{a}_{drag} = \frac{1}{2} C_D \frac{A}{m} \rho v^2 \tag{5}$$

A summary of the design choices is presented in Table 1, and Figure 2 shows the top-level architectural design for the calibration.

Table 1: Summary of the design choices and test cases.

Longitude grid	80 (0°, 360°)	
Latitude grid	40 (−90°, 90°)	
Time grid	$144 \cdot 31$ (1 month)	
PCA	10 components	
Interpolation	RBF for calibration Lagrange for propagation	
Perturbations	Non-spherical harmonics 64x64 Solid tides Third body: Moon, Sun, J2-Moon Cannonball SRP Drag force	
	Case 1	Case 2
Training period	Jan. 2019	Mar. 2022
Predicting period	Feb. 2019	Apr. 2022
Fitting interval	21^{th}-24^{th}	21^{th}-24^{th}
Propagation interval	24^{th}-31^{th}	24^{th}-31^{th}
Satellites	GRACE-FO-1	Swarm-C

3. RESULTS

In this section, the findings of the present study on calibrating NRLMSISE-00 to thermospheric density observations are presented. The analysis is divided into three main subsections, each focusing on a specific aspect of the study. In the first subsection, we discuss the main modes of the PCA, its physical meaning and its temporal variation. In the second subsection, we present the results of our density calibration and prediction, including the methods and metrics used to evaluate the accuracy of the predictions. Finally, in the third subsection, we detail the results of our orbital propagation with calibrated NRLMSISE-00, and how it was used to improve the accuracy of our predictions. Overall, our results demonstrate the strengths of using a calibrated version of NRLMSISE-00 with a PCA to both predict the density over one month and propagate the orbits over one week.

3.1. Principal Component Analysis

In this subsection, the results of a principal component analysis (PCA) and its application to the dataset are presented. PCA was performed on the dataset with 10 components, which were chosen as it retains $92.89\,\%$ of the energy of the system (see Figure 1). Figure 3 shows the shape of the spatial modes obtained, very similar to the modes found in literature [29]. However, there are several differences. First, the time grid: it is broader in this analysis, as the work referenced only analysed one day, while a full month is analysed here. Second, the use of indices a_P and $F_{10.7}$ that are coherent with real observations. Third, the use of a bi-dimensional spatial grid, and scaling altitude with Equation 1, instead of creating a coarser grid in three dimensions.

Each of the 10 components extracted from the PCA has a physical meaning associated with features of the atmosphere. For example, modes 1 and 2 correspond with the diurnal migrating solar tide, and modes 4 and 5 correspond with the semi-diurnal migrating solar tide (see Figure 3). Modes 3, 6, and 9 correspond with a slower, semi-monthly, variation, and modes 3 and 6 seem to be in phase opposition, according to the pattern in Figure 3. These results seem to indicate that the PCA correctly captures the relevant patterns and relationships over the sampling period. These slower variating modes do not appear in the work by Mehta and Linares [29], due to the brief sampling period.

3.2. Density calibration and prediction

In this subsection, the results of the WLSE used for density calibration are described, including the residuals, covariance and correlation analysis. The calibrated density values are presented, and their precision is evaluated through comparison with Swarm-C density data. The ability of the model to predict density values at unobserved locations and altitudes based on the calibrated density values is demonstrated. The results of this study indicate the effectiveness of the density calibration and prediction approach in providing reliable and accurate density estimates for use in a variety of atmospheric and space-related applications.

In the first step, residuals have been scaled with the standard deviation of the observations $\sigma_{observations}$. During calibration, this parameter was chosen to ensure that the weighted RMS is exactly 1, making the fit more consistent. The mean and standard deviation obtained with this scaling parameter are 0 and 1, respectively. It indicates that the calibration is consistent and that the standard deviation has been chosen correctly.

Furthermore, the calibrated model should be compared using an unbiased metric. An example of unbiased metrics is the mean and the standard deviation of the ratio between the observed and computed densities in a logarithmic scale [6, 7]. The main metrics used to compute the residuals and evaluate the fit are the ones described by Bruinsma et al. [6]:

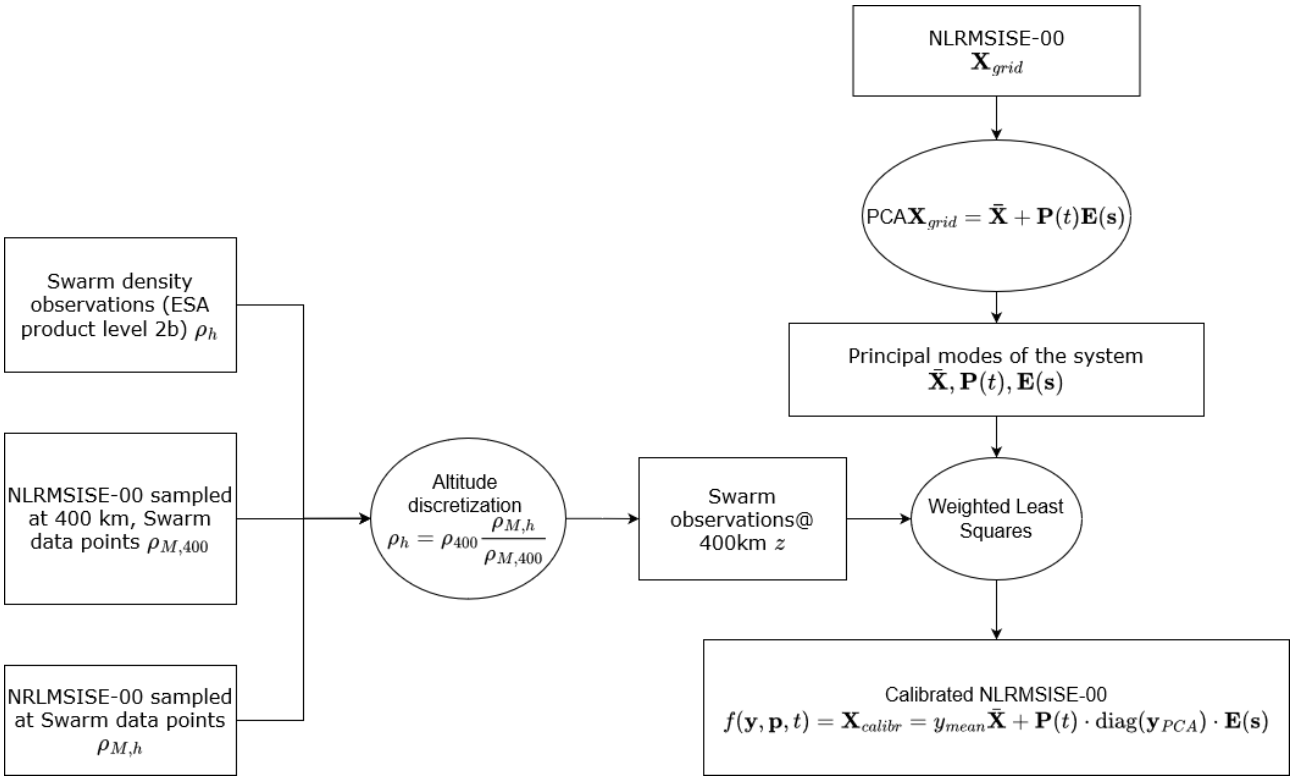

Figure 2: Top level flow-chart of the calibration process.

$$\mu = \exp\left(\text{MEAN}\left(\ln\left(\frac{\rho_{observations}}{\rho_{model}}\right)\right)\right) \quad (6)$$

$$\sigma = \exp\left(\text{STD}\left(\ln\left(\frac{\rho_{observations}}{\rho_{model}}\right)\right) - 1\right) \cdot 100 \quad (7)$$

These metrics take into account both the magnitude and distribution of the residuals and have been argued as a fair assessment metric [6].

Table 2: Mean and standard deviation for both cases, computed using Equation 6 and Equation 7.

	Case 1	Case 2
	Calibration	
NRLMSISE-00	0.51, 51.16 %	0.81, 15.19 %
Calibrated	1.00, 47.19 %	1.00, 13.53 %
	Prediction	
NRLMSISE-00	0.58, 35.70 %	0.83, 22.70 %
Calibrated	1.04, 34.14 %	1.00, 25.60 %

Table 2 shows the mean and standard deviation from Equation 6 and Equation 7 for all cases. This metric, not dependent on any ad-hoc parameter (such as $\sigma_{observations}$, the parameter used to validate the calibration), shows that the calibrated model mirrors the residuals for almost all cases.

Figure 4 shows the logarithm of the ratio of the residuals for January 2019. For this case, the standard deviation has been slightly reduced during the calibration too: from $51.16\,\%$ to $47.19\,\%$. During the medium solar activity (March 2022), NRLMSISE-00 is closer to Swarm-C density observations, as the higher mean and standard deviation in Table 2 show. Furthermore, the calibrated model exactly fits the observations and reduces the standard deviation.

Calibration of the model has been performed using the logarithm of Swarm-C GNSS-derived density observations as measurements. When the model is calibrated on the density, the calibration performed slightly worse: a mean of 0.9681 was obtained on the ratio and a standard deviation of $49.95\,\%$. As the logarithm of the density is represented by a normal distribution, it was expected that the calibration on the logarithm would have better results.

The correlation matrix of the estimation process and the ratio between each parameter and its variance are shown in Figure 6. For every parameter but parameters 5 and 9, which correspond to modes 6 and 10, the parameter value is at least one order of magnitude higher than the estimated variance, which provides confidence in the estimated parameters. Furthermore, the correlation matrix shows an inverse relationship between parameters 0 and 1, 3 and 4, and a strong direct relationship between parameters 6 and 7, and 0, 1, 6, and 7. The inverse relationship can be explained as the parameters are opposite in phase, as it can be seen in Figure 3, so the WLSE keeps the physical properties of the method. Figure 6 shows a direct correlation around $30\,\%$ between

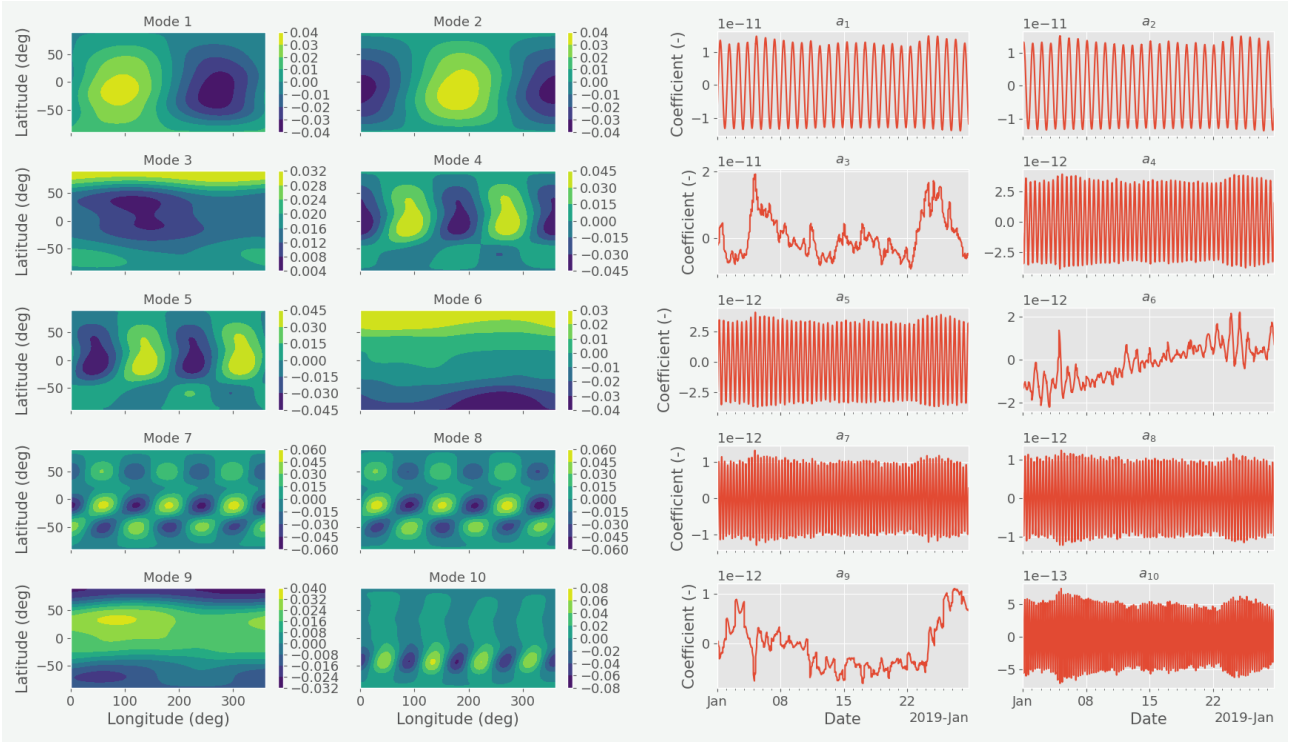

Figure 3: Spatial and temporal evolution of the 10 principal components or modes of NRLMSISE-00 during January 2019.

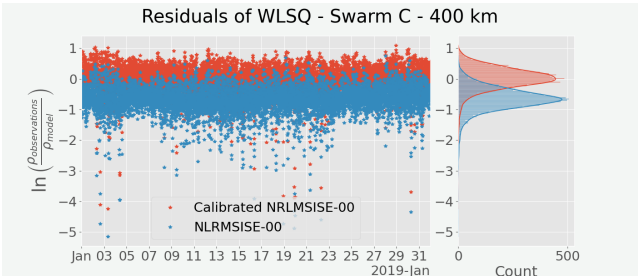

Figure 4: Relative residuals during January 2019.

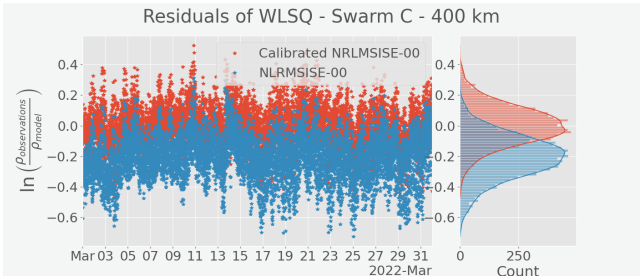

Figure 5: Relative residuals during March 2022.

parameters 0, 1, 6, and 7, which are modes with a frequency of 24 h and 8 h. The calibration was also performed using coarser grids in time, obtaining worse calibration and correlation output.

The calibration has been performed using observations during January 2019, low solar activity, and during March 2022, medium-high solar activity. Therefore, it is of interest to predict the density values during the following time interval while using prior calibration $\mathbf{y}$. To do so, PCA is performed again on NRLMSISE-00, and matrices $\bar{\mathbf{X}}(\mathbf{s})$, $\mathbf{E}(\mathbf{s})$, and $\mathbf{P}(t)$ have been computed in February 2019 and April 2022. It is assumed that all solar indices and other NRLMSISE-00 inputs are available. However, no density observations have been used during the propagation, and parameters $\mathbf{y}$ are the output of prior calibration. As the residuals show in Figure 7, the model is fitted to Swarm-C observations with a mean value of almost one, and the standard deviation is reduced. The standard deviation is lower for the residuals in February than for the residuals in January, due to NRLMSISE-00 being closer to the residuals during the testing data. Density has also been predicted during April 2022, and a similar trend can be observed for the medium solar activity case in Figure 8: the calibrated model is fitted to Swarm-C observations using data from March 2022, and the mean of the density ratio is close to 1.0 in April 2022. However, the standard deviation increases for the calibrated model. This might be due to the particular pattern shown by the ratio of Swarm-C observation and the NRLMSISE-00 model during April 2022.

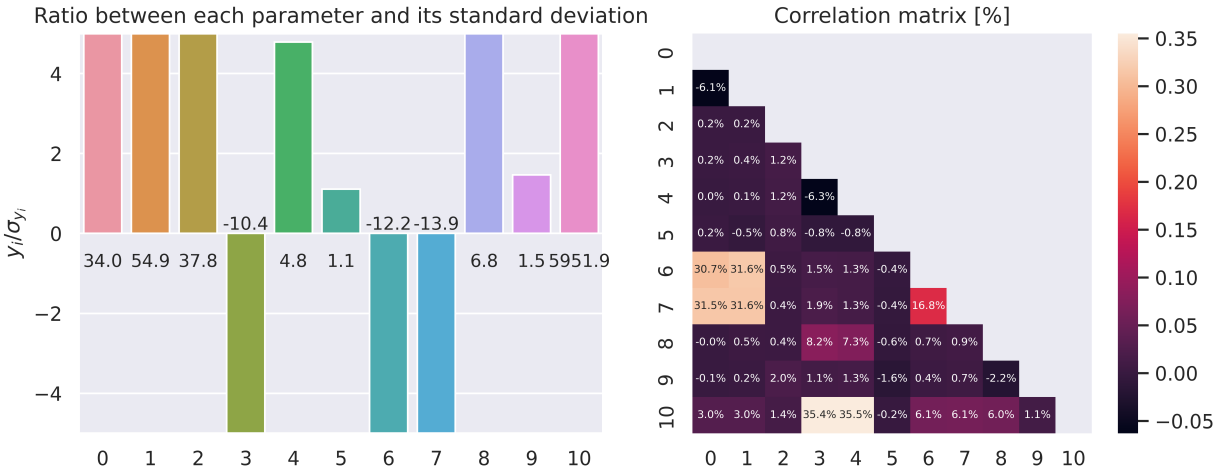

Figure 6: Left: ratios of the estimated parameters and their standard deviation, indicating the parameters' significance. Right: correlation matrix of the parameters.

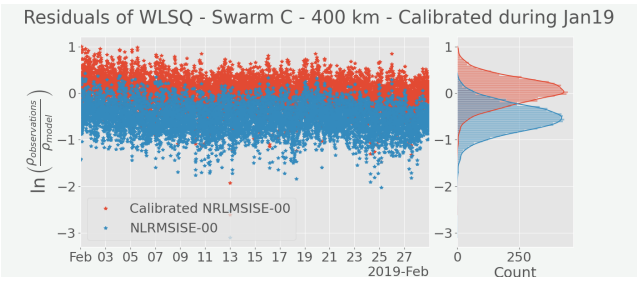

Figure 7: Relative residuals during February 2019 calibrating during January 2019.

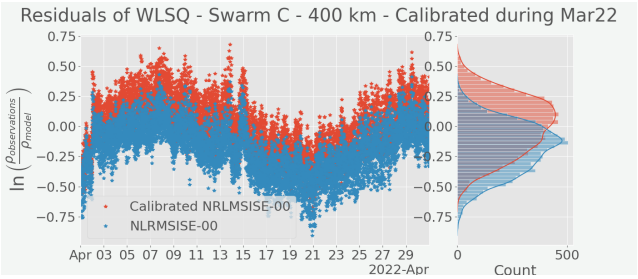

Figure 8: Relative residuals during April 2022 calibrating during March 2022.

3.3. Orbital propagation with calibrated NRLMSISE-00

This subsection deals with the propagation of two test orbits after they have undergone a fit to POD observations. The fit process, which adjusts initial orbital parameters to better match observed data, is a crucial step in orbit determination. Propagating these orbits allows for a better understanding of their behaviour and potential deviations from the fitted parameters. The test orbits examined in this subsection include two satellites: GRACE-FO-1, and Swarm-C.

Figure 9 shows the propagation of satellite GRACE-FO-1 from 21st to 31th of January 2019. From the 21st to the 24st, an orbital fit was performed in the orbit, so error accumulates from the 24th onwards. There are four plots: two corresponding to the propagation with the fitted initial parameters, and two corresponding to propagating with one density model with the fitted parameters of the other. The initial parameters obtained with the fit for both cases are collected in Table 3. It can be observed that the best fit is obtained when propagating with the same density model as the fitting method. However, the C_D coefficient is more realistic to high-fidelity estimations [26, 27] when fitting with the calibrated model. Worst behaviour is obtained by the calibrated model when propagating with an unrealistic C_D, while NRLMSISE-00 performance with a realistic C_D is the second worst. This pattern changes when propagating Swarm-C satellite, as Figure 11 shows. When propagating the same satellite whose densities have been assimilated, the calibrated model outperforms NRLMSISE-00 when using the C_D that does not correspond with their model.

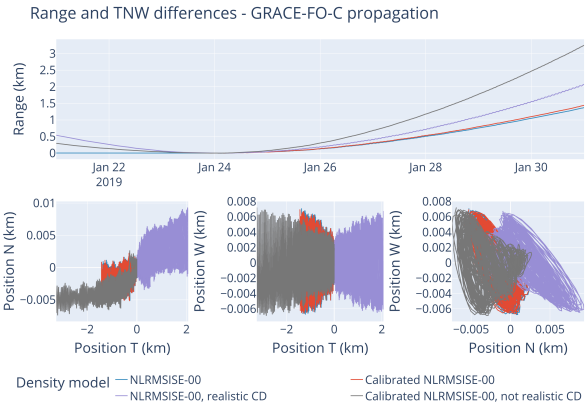

Figure 9: Propagation of GRACE-FO-1 satellite during January 2019.

Table 3: Initial parameters obtained during orbital fit, for both cases. Position and velocity in inertial frame of reference.

	Initial position [km]			Initial velocity [km s^{-1}]			C_D	C_D^{ref}	C_R
	x	y	z	x	y	z			
Case 1									
Swarm-C, NRLMSISE-00	-1011.25	481.69	-6730.36	5.557	-5.090	-1.200	1.304	3.167	0.508
Swarm-C, Calibrated	-1011.26	481.69	-6730.36	5.557	-5.090	-1.200	2.504	3.167	0.478
GRACE-FO-1, NRLMSISE-00	-1918.84	-795.93	-6569.05	-6.492	-3.194	2.295	2.912	1.512	1.204
GRACE-FO-1, Calibrated	-1918.84	-795.93	-6569.05	-6.492	-3.194	2.295	2.821	2.912	1.279
Case 2									
Swarm-C, NRLMSISE-00	2558.01	-3175.75	6780.53	1.991	7.390	0.288	2.25	3.133	0.49
Swarm-C, Calibrated	2558.07	-3175.53	6780.53	1.991	7.389	0.288	2.76	3.133	0.53
GRACE-FO-1, NRLMSISE-00	2202.62	2454.30	-6025.04	4.266	5.136	3.659	2.91	2.871	0.94
GRACE-FO-1, Calibrated	2202.62	2454.30	-6025.04	4.266	5.136	3.659	3.43	2.871	0.92

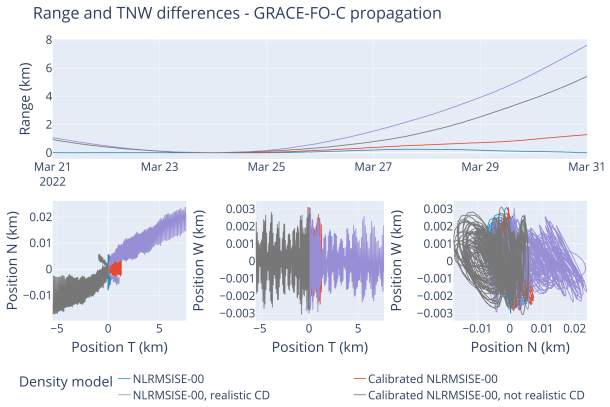

Figure 10: Propagation of GRACE-FO-1 satellite during March 2022.

The same satellites have also been propagated during March 2022, in a period with higher solar activity, and thus higher values for the density and the drag force. The result of the propagation is shown in Figure 12 and Figure 10 for Swarm-C and GRACE-FO-1, respectively. The range of the propagation is more than two times the propagation with low solar activity. Furthermore, the orbital fit with NRLMSISE-00 can fit the dynamical model not only during training (21st to 24th) but also during propagation. The calibrated model with a not realistic C_D (grey curve) performs better than NRLMSISE-00 with a realistic C_D (purple curve) for both satellites.

When using a fixed area geometry in the satellite, the effect of calibration of density and orbital fit can be blended, and implementing a panel model to obtain the drag coefficient instead of estimating it could improve the results. One advantage of this method is that when POD ephemeris of the orbit is not known, and if the conditions of the satellite are close to Swarm-C orbit, the method may be better than using the NRLMSISE-00 model.

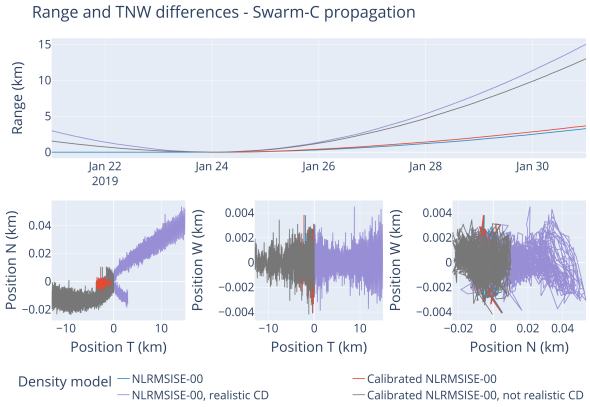

Figure 11: Propagation of Swarm-C satellite during January 2019.

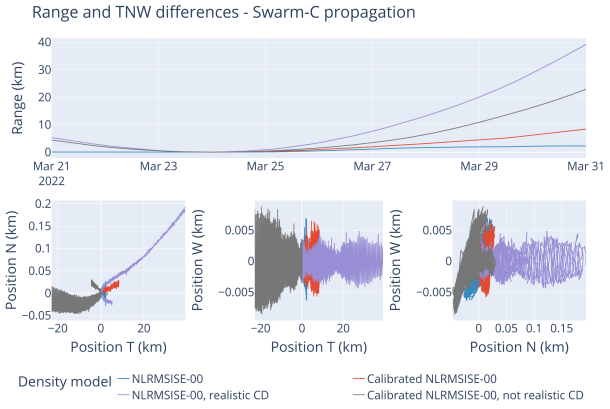

Figure 12: Propagation of Swarm-C satellite during March 2022.

4. SUMMARY AND OUTLOOK

The present document shows the preliminary results of ongoing work as part of a Master's Thesis at TUDelft in collaboration with GMV. In this work, a calibration procedure for NRLMSISE-00 has been proposed, and its prediction capabilities for propagation over ten days have been tested. A PCA of NRLMSISE-00 shows that the main modes of NRLMSISE-00 correspond to physical phenomena and capture most of the energy of the system. The complexity of the problem is reduced while also retaining $92.89\,\%$ of the density grid information. A simple, but effective WLSE algorithm has been proposed as a means of reducing the over-prediction of NRLMSISE-00 when comparing it to GNSS-derived thermospheric density observations. The calibration has been validated, and two prediction tests have determined that is feasible to use this method to obtain values of the density in the close future. Finally, the propagation of orbits using the calibrated model has been tested using four different test cases with fixed-area satellite geometry. As the satellites that have been propagated, namely Swarm-C and GRACE-FO-1, have a known POD orbit, an orbital fit has been performed prior to the propagation. The orbital fit apparently overshadows the benefits of the calibration, as both C_D and density affect the drag acceleration in the same way. However, a more realistic C_D coefficient is drawn from the orbital fit with the calibrated model, and the method might be beneficial for satellites without precisely known orbits.

Current and future steps of this ongoing work include: to design of a test case with a high-fidelity geometry of a satellite; including covariance realism characterization of the orbits; performing a sensitivity analysis on the orbital propagation and the calibrated model parameters; and assessing the prediction capabilities of the orbit in cases where the solar indices $F_{10.7}$ and a_P are not observed but predicted. Being able to accurately characterize and propagate LEO orbits and to reduce the uncertainty on the drag contribution would hugely benefit any space application. In particular, as LEO is the most crowded region in space, every SSA and STM applications.

REFERENCES

1. G. Bowden. Orbit-localised thermosphere density prediction using a Kalman filter based calibration of empirical models. *Acta Astronautica*, 197:6–13, 2022.
2. B. Bowman, W. K. Tobiska, F. Marcos, C. Huang, C. Lin, and W. Burke. A new empirical thermospheric density model JB2008 using new solar and geomagnetic indices. In *AIAA/AAS Astrodynamics Specialist Conference and Exhibit*. American Institute of Aeronautics and Astronautics, 2008. doi:10.2514/6.2008-6438.
3. B. R. Bowman, W. K. Tobiska, F. A. Marcos, and C. Valladares. The JB2006 empirical thermospheric density model. *Journal of Atmospheric and Solar-Terrestrial Physics*, 70(5):774–793, 2008. doi:10.1016/j.jastp.2007.10.002.
4. S. Bruinsma. The DTM-2013 thermosphere model. *Journal of Space Weather and Space Climate*, 5:A1, 2015.
5. S. Bruinsma and C. Boniface. The operational and research DTM-2020 thermosphere models. *Journal of Space Weather and Space Climate*, 11:47–1, 2021.
6. S. Bruinsma, E. Sutton, S. Solomon, T. Fuller-Rowell, and M. Fedrizzi. Space weather modeling capabilities assessment: Neutral density for orbit determination at low Earth orbit. *Space Weather*, 16 (11):1806–1816, 2018.
7. S. Bruinsma, C. Boniface, E. K. Sutton, and M. Fedrizzi. Thermosphere modeling capabilities assessment: geomagnetic storms. *Journal of Space Weather and Space Climate*, 11:12, 2021.
8. E. Doornbos. *Thermospheric density and wind determination from satellite dynamics*. PhD thesis, Technische Universiteit Delft, 2011.
9. E. Doornbos and H. Klinkrad. Modelling of space weather effects on satellite drag. *Advances in Space Research*, 37(6):1229–1239, 2006. doi:10.1016/j.asr.2005.04.097.
10. E. Doornbos, H. Klinkrad, R. Scharroo, and P. Visser. Thermosphere density calibration in the orbit determination of ERS-2 and Envisat. In *Envisat Symposium*, 2007.
11. E. Doornbos, H. Klinkrad, and P. Visser. Use of two-line element data for thermosphere neutral density model calibration. *Advances in Space Research*, 41(7):1115–1122, 2008. doi:10.1016/j.asr.2006.12.025.
12. J. Emmert, D. Drob, J. Picone, D. Siskind, J. Jones, M., M. Mlynczak, P. Bernath, X. Chu, E. Doornbos, B. Funke, L. Goncharenko, M. Hervig, M. Schwartz, P. Sheese, F. Vargas, B. Williams, and T. Yuan. NRLMSIS 2.0: A whole-atmosphere empirical model of temperature and neutral species densities. *Earth and Space Science*, 8(3), 2021. doi:10.1029/2020EA001321.
13. S. D. O. ESA. Esa's annual space environment report. Technical report, 2021.
14. E. Forootan, S. Farzaneh, C. Lück, and K. Vielberg. Estimating and predicting corrections for empirical thermospheric models. *Geophysical Journal International*, 218(1):479–493, 2019. doi:10.1093/gji/ggz163.
15. E. Forootan, S. Farzaneh, M. Kosary, M. Schmidt, and M. Schumacher. A simultaneous calibration and data assimilation (C/DA) to improve NRLMSISE00 using thermospheric neutral density (TND) from space-borne accelerometer measurements. *Geophysical Journal International*, 224(2):1096–1115, 2020. doi:10.1093/gji/ggaa507.
16. E. Friis-Christensen, H. Lühr, D. Knudsen, and R. Haagmans. Swarm – an earth observation mission investigating geospace. *Advances in Space Research*, 41(1):210–216, 2008.
17. D. J. Gondelach and R. Linares. Real-time thermospheric density estimation via two-line element data assimilation. *Space Weather*, 18(2), 2020. doi:10.1029/2019sw002356.
18. D. J. Gondelach and R. Linares. Real-time thermospheric density estimation via radar and GPS tracking data assimilation. *Space Weather*, 19(4), 2021. doi:10.1029/2020sw002620.
19. C. He, Y. Yang, B. Carter, E. Kerr, S. Wu, F. Deleflie, H. Cai, K. Zhang, L. Sagnières, and R. Norman. Review and comparison of empirical thermospheric mass density models. *Progress in Aerospace Sciences*, 2018. doi:10.1016/j.paerosci.2018.10.003.
20. A. E. Hedin. MSIS-86 thermospheric model. *JGR. Journal of geophysical research. Part D, Atmospheres*, 92(5):4649–4662, 1987.
21. ISO Central Secretary. Standard atmosphere. Standard ISO/TC 20/SC 6 2533:1975, International Organization for Standardization, Geneva, CH, 1975. URL https://www.iso.org/standard/7472.html.
22. I. Kim, D. J. Pawlowski, A. J. Ridley, and D. S. Bernstein. Localized data assimilation in the ionosphere-thermosphere using a sampled-data unscented Kalman filter. In *2008 American Control Conference*, pages 1849–1854. IEEE, 2008.
23. H. Klinkrad. *Space Debris: Models and Risk Analysis*. Springer-Verlag Berlin Heidelberg, 2006. ISBN 978-3-540-25448-5. doi:10.1007/3-540-37674-7.
24. R. J. Licata, P. M. Mehta, and W. K. Tobiska. Impact of space weather driver forecast uncertainty on drag and orbit prediction. volume 175, pages 1941–1959. Univelt Inc., 2020.
25. R. J. Licata, P. M. Mehta, W. K. Tobiska, and S. Huzurbazar. Machine-learned HASDM thermospheric mass density model with uncertainty quantification. *Space Weather*, 20(4), 2022. doi:10.1029/2021sw002915.

26. G. March, E. Doornbos, and P. Visser. High-fidelity geometry models for improving the consistency of champ, grace, goce and swarm thermospheric density data sets. *Advances in Space Research*, 63 (1):213–238, 2019.

27. G. March, T. Visser, P. Visser, and E. Doornbos. Champ and goce thermospheric wind characterization with improved gas-surface interactions modelling. *Advances in Space Research*, 64(6):1225–1242, 2019.

28. T. Matsuo, M. Fedrizzi, T. Fuller-Rowell, and M. Codrescu. Data assimilation of thermospheric mass density. *Space Weather*, 10(5), 2012. doi:10.1029/2012SW000773.

29. P. M. Mehta and R. Linares. A methodology for reduced order modeling and calibration of the upper atmosphere. *Space Weather*, 15(10):1270–1287, 2017. doi:10.1002/2017SW001642.

30. O. Montenbruck and E. Gill. *Satellite Orbits: Models, Methods and Applications*. Springer Science & Business Media, 2005. doi:10.1007/978-3-642-58351-3.

31. A. V. Morozov, A. J. Ridley, D. S. Bernstein, N. Collins, T. J. Hoar, and J. L. Anderson. Data assimilation and driver estimation for the Global Ionosphere–Thermosphere Model using the ensemble adjustment Kalman filter. *Journal of Atmospheric and Solar-Terrestrial Physics*, 104: 126–136, 2013.

32. C. Pardini, K. Moe, and L. Anselmo. Thermospheric density model biases at the 23rd sunspot maximum. *Planetary and Space Science*, 67(1):130–146, 2012. doi:10.1016/j.pss.2012.03.004.

33. D. Pérez, B. Wohlberg, T. A. Lovell, M. Shoemaker, and R. Bevilacqua. Orbit-centered atmospheric density prediction using artificial neural networks. *Acta Astronautica*, 98:9–23, 2014. doi:10.1016/j.actaastro.2014.01.007.

34. J. M. Picone, A. E. Hedin, D. P. Drob, and A. C. Aikin. NRLMSISE-00 empirical model of the atmosphere: Statistical comparisons and scientific issues. *Journal of Geophysical Research: Space Physics*, 107(A12):SIA 15–1–SIA 15–16, 2002. doi:10.1029/2002ja009430.

35. L. Qian, A. Burns, B. Emery, B. Foster, G. Lu, A. Maute, A. Richmond, R. Roble, S. Solomon, and W. Wang. The NCAR TIE-GCM: A community model of the coupled thermosphere/ionosphere system. 9780875904917: 73–83, 2014. doi:10.1002/9781118704417.ch7.

36. A. Ridley, Y. Deng, and G. Toth. The global ionosphere–thermosphere model. *Journal of Atmospheric and Solar-Terrestrial Physics*, 68(8): 839–864, 2006.

37. D. Sáez Bo and D. Escobar Antón. Performance characterization of sst systems based on radar sensors. Master's thesis, Carlos III University of Madrid, 2018.

38. M. F. Storz, B. R. Bowman, M. J. I. Branson, S. J. Casali, and W. K. Tobiska. High accuracy satellite drag model (HASDM). *Advances in Space Research*, 36(12):2497–2505, 2005. doi:10.1016/j.asr.2004.02.020.

39. D. A. Vallado and D. Finkleman. A critical assessment of satellite drag and atmospheric density modeling. *Acta Astronautica*, 95:141–165, 2014. doi:10.1016/j.actaastro.2013.10.005.

40. J. van den IJssel, E. Doornbos, E. Iorfida, G. March, C. Siemes, and O. Montenbruck. Thermosphere densities derived from Swarm GPS observations. *Advances in Space Research*, 65(7):1758–1771, 2020. doi:10.1016/j.asr.2020.01.004.

41. P. Virtanen, R. Gommers, T. E. Oliphant, M. Haberland, T. Reddy, D. Cournapeau, E. Burovski, P. Peterson, W. Weckesser, J. Bright, S. J. van der Walt, M. Brett, J. Wilson, K. J. Millman, N. Mayorov, A. R. J. Nelson, E. Jones, R. Kern, E. Larson, C. J. Carey, İ. Polat, Y. Feng, E. W. Moore, J. VanderPlas, D. Laxalde, J. Perktold, R. Cimrman, I. Henriksen, E. A. Quintero, C. R. Harris, A. M. Archibald, A. H. Ribeiro, F. Pedregosa, P. van Mulbregt, and SciPy 1.0 Contributors. SciPy 1.0: Fundamental Algorithms for Scientific Computing in Python. *Nature Methods*, 17:261–272, 2020. doi:10.1038/s41592-019-0686-2.

42. P. Visser, E. Doornbos, J. van den IJssel, and J. Teixeira da Encarnação. Thermospheric density and wind retrieval from swarm observations. *Earth, Planets and Space*, 65(11):1319–1331, 2013.

43. M. E. Wall, A. Rechtsteiner, and L. M. Rocha. *Singular Value Decomposition and Principal Component Analysis*, pages 91–109. Springer US, Boston, MA, 2003. ISBN 978-0-306-47815-4. doi:10.1007/0-306-47815-3_5.

44. L. Zeitler, A. Corbin, K. Vielberg, S. Rudenko, A. Löcher, M. Bloßfeld, M. Schmidt, and J. Kusche. Scale factors of the thermospheric density: A comparison of satellite laser ranging and accelerometer solutions. *Journal of Geophysical Research: Space Physics*, 126(12), 2021. doi:10.1029/2021JA029708.